

Resolution improvement by single-exposure superresolved interferometric microscopy with a monochrome sensor

Alejandro Calabuig,¹ Javier Garcia,¹ Carlos Ferreira,¹ Zeev Zalevsky,² and Vicente Micó^{1,*}

¹*Departamento de Óptica, University of Valencia, C/Doctor Moliner 50, 46100 Burjassot, Spain*

²*School of Engineering, Bar-Ilan University, 52900 Ramat-Gan, Israel*

*Corresponding author: vicente.mico@uv.es

Received July 26, 2011; revised September 21, 2011; accepted September 22, 2011;
posted September 23, 2011 (Doc. ID 151830); published October 26, 2011

Single-exposure superresolved interferometric microscopy (SESRIM) by RGB multiplexing has recently been proposed as a way to achieve one-dimensional superresolved imaging in digital holographic microscopy by a single-color CCD snapshot [Opt. Lett. **36**, 885 (2011)]. Here we provide the mathematical basis for the operating principle of SESRIM, while we also present a different experimental configuration where the color CCD camera is replaced by a monochrome (B&W) CCD camera. To maintain the single-exposure working principle, the object field of view (FOV) is restricted and the holographic recording is based on image-plane wavelength-dispersion spatial multiplexing to separately record the three bandpass images. Moreover, a two-dimensional extension is presented by considering two options: time multiplexing and selective angular multiplexing. And as an additional implementation, the FOV restriction is eliminated by varying the angle between the three reference beams in the interferometric recording. Experimental results are reported for all of the above-mentioned cases. © 2011 Optical Society of America

OCIS codes: 090.4220, 100.2000, 100.6640, 180.3170.

1. INTRODUCTION

Optical imaging systems have a diffraction-limited resolution due to the wave nature of light [1]. Because of the bandpass limitation of imaging systems in terms of spatial frequencies, every optical system provides a limited transversal resolution (ρ) that is proportional to its numerical aperture (NA) and the illumination wavelength (λ) according to $\rho = k\lambda/\text{NA}$ for imaging systems and assuming that no other factors (geometrical resolution and noise) are present. The value of the proportional constant k depends on the imaging system configuration, but it usually has a value of 0.82 for coherent imaging systems having circular apertures [2,3]. However, that value depends on the shape and transmittance of the aperture and on the role of the phase in recording. Obviously, the higher the NA, the better the resolution limit. The theoretical best value of the resolution limit that can be reached is $k\lambda$ for air-immersed imaging systems incoming from a theoretical maximum NA value equal to 1; practical values are a little bit lower (some commercial objectives can get to a value of 0.95). Optical superresolution is concerned the capability to overcome the resolution limit provided by diffraction without changing the geometrical properties of the optical imaging system, that is, without affecting its NA value [4].

In particular, digital holographic microscopy (DHM) allows noncontact (no sample damage), noninvasive (no need for stained samples), static (no moving components), real-time (on-line control), and full-field (nonscanning) imaging of different samples ranging from electromechanical components to biological specimens. DHM [5–7] combines the advantages provided by digital holography concerning digital postprocessing of the recorded hologram with the high image quality

provided by optical microscopy, while it avoids the limited resolution imposed by the finite number and size of the pixels in the digital sensor. Because of its versatility, it has been applied to various applications such as real-time polarization microscopy imaging [8], aberration lens compensation [9], particle tracking [10], extended depth-of-field imaging [11], quantitative phase contrast imaging [12], three-dimensional dynamic analysis of cells [13], and others.

In DHM and for a fixed illumination wavelength, the transversal resolution limit is usually defined by the NA of the microscope objective itself. As Abbe pointed out [1], high-resolution imaging demands high-NA lenses. But high-NA microscope objectives have a small field of view (FOV), a short working distance, and a reduced depth of focus in comparison with low-NA lenses. Leaving aside the depth-of-field reduction, the rest of the disadvantages persist and can be a drawback depending on the application.

Optical superresolution in DHM has been widely studied mainly in the past decade [14–34]. The underlying principle concerning all of those approaches is to illuminate the input object with a set of tilted beams. Then, several objects' orientations containing different spatial-frequency information are angularly multiplexed at different domains, such as time [14,15,17–31,33], coherence [16,19,34], and polarization [24,32]. As a result, a synthetic numerical aperture (SNA) is obtained presenting an improved cut-off frequency, thus improving the spatial resolution limit, in comparison with those values provided by the same optical system without applying the superresolution approach. The recovery of each elementary aperture is performed by holographic recording, and the synthetic aperture (SA) is assembled in a latter digital postprocessing stage. Numerical manipulation concerning the

coherent addition of each elementary aperture into a single expanded SA is described in detail in Refs. [29,31,35].

However, most of the SA superresolution methods in DHM are based on the sequential implementation of the tilted beam illumination stage [14,15,17–31,33]. This time multiplexing principle prevents the study of nonstatic objects, nonstatic at least during the duration of the illumination stage implementation (typically from some tenths of a second to a few seconds depending on system complexity and involved hardware). Recently proposed, single-exposure superresolved interferometric microscopy (SESRIM) by RGB multiplexing allows one-dimensional (1D) superresolution imaging in DHM using a single illumination shot and a single-color CCD capture [34]. SESRIM combines angular with wavelength multiplexing to transmit in parallel three bandpass images of the input object through the objective lens. The holographic detection scheme is based on the use of a color CCD, where the three RGB channels are separately analyzed to recover the three-object color-coded bandpass images. Finally, a 1D superresolution imaging is obtained by proper digital management of the information contained in the three bandpass images. The single-exposure superresolution capability enables the study of real-time events and becomes a highly attractive and applicable field of research.

In this manuscript, we present a modification of our previously reported SESRIM technique [34]. Instead of using a color CCD, a monochrome (B&W) CCD camera records, in a single CCD capture, the three-object bandpass images in the form of a multiplexed hologram coming from the addition of three wavelength-dependent subholograms. Thus, the resolution is not penalized by signal sampling at the image plane because the B&W CCD camera uses all the disposable pixels (not like a color CCD with a Bayer filter). To achieve nonoverlapping and separate recovery of the color-coded bandpass images at the image plane, both image-plane spatial multiplexing as well as FOV restriction are performed by wavelength dispersion provided a 1D diffraction grating placed after

the microscope lens and a limiting slit attached to the input object, respectively. After a single hologram recording, the spatial-frequency content incoming from each bandpass image is properly managed to synthesize an expanded SA that provides a 1D superresolved imaging by simply Fourier transforming the information contained in the generated SA. Both in this manuscript and in SESRIM by RGB multiplexing [34], the use of different wavelengths should be interpreted as coherence coding rather than wavelength coding, and in both manuscripts color information about the input sample is sacrificed to achieve superresolution effect derived from a single CCD recording.

The manuscript is organized as follows. Section 2 presents both a qualitative description and the mathematical background of SESRIM. Section 3 experimentally validates SESRIM using image-plane wavelength-dispersion multiplexing and its evolutions [two-dimensional (2D) extension and FOV restriction elimination] by providing different experiments for 1D and 2D cases. Section 4 concludes the paper.

2. THEORETICAL DESCRIPTION OF SESRIM

A. Qualitative System Description and Analysis of Synthetic Aperture Generation

The experimental setup is depicted in Fig. 1. Three Mach-Zehnder interferometers are assembled and matched in the optical path for three different laser beams: red (R), green (G), and violet (V) wavelengths. In the imaging arm, the three laser beams simultaneously illuminate the input plane with different illumination directions. In the SESRIM method [34], the R beam illuminates in on-axis mode the input object while the G and V beams reach coplanar but obliquely the object at angles θ_G and θ_V , respectively (see Fig. 1). This angular- and wavelength-multiplexing in the illumination allows the transmission through the microscope lens of three independent color-coded bandpass images containing different spectral range of the input object. Those three bandpass images interfere with a set of three coherent reference beams that are

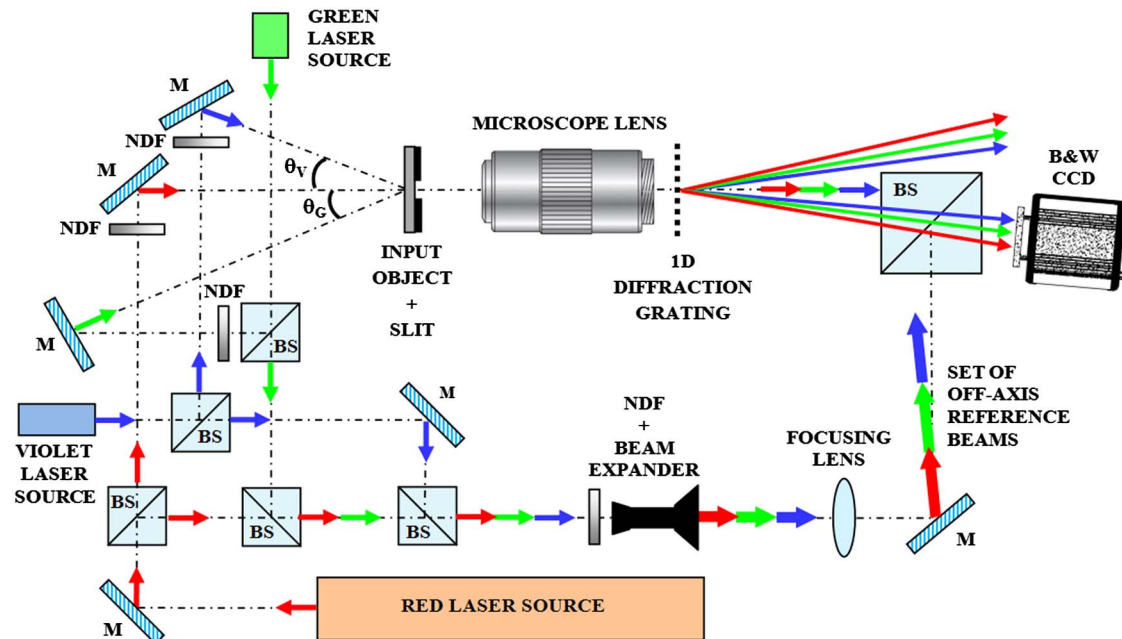


Fig. 1. (Color online) Upper view of the experimental setup for SESRIM by image-plane wavelength-dispersion multiplexing: M, mirror; NDF, neutral density filter; and BS, beamsplitter.

mutually incoherent. The three reference beams are mixed together in the reference arm of the interferometric setup having the same propagation direction, that is, they are collinear. Finally, the three reference beams are introduced in the off-axis mode at the image plane by slightly tilting the reference mirror, and a B&W CCD records three independent holograms, one for each illumination wavelength, at the image output plane.

Under these conditions, the complex amplitude incoming from the three transmitted bandpass images cannot be recovered by filtering one of the hologram diffraction orders, because the three bandpass images overlap at the image plane (the three reference beams are collinear). To allow complex amplitude distribution recovery, SESRIM by RGB multiplexing [34] retrieves, in a single-color CCD capture, each transmitted color-coded bandpass image by looking independently at the three RGB CCD channels. Now, this paper presents a different way to accomplish complex amplitude bandpass image recovery: a 1D diffraction grating disperse in wavelength the three color-coded bandpass images at the image plane by using one of the grating diffraction orders. As a consequence, the bandpass images reach the image plane in a different spatial position and can be recovered by spatial filtering at the image plane, assuming that the B&W CCD has a sensitive area that is wide enough to record the three dispersed bandpass images. However, if the angular separation provided by the 1D grating does not spatially separate the bandpass images completely, overlapping will still happen. Because the CCD size is only a few millimeters, additional FOV limitation is needed to guarantee nonoverlapping of the different color-coded bandpass images. To allow this, a 1D slit is placed in contact with the input object at the input plane.

In addition, the experimental setup includes several mirrors (M) and nonpolarizing beamsplitter cubes (BS) to assemble the three interferometers, some neutral density filters (NDF) to equalize beam intensity and maximize fringe contrast in the holographic recording, a beam expander in the reference arm to illuminate the whole CCD area with the reference beams, and a focusing lens in the reference arm to allow divergence compensation between both interferometric beams. Finally, notice that the CCD is slightly tilted at the recording plane (see Fig. 1) in order to minimize misfocus of the bandpass images due to the lack of orthogonality between the imaging beams and the CCD by the action of the 1D grating. The CCD is placed perpendicular to the G bandpass image, thus minimizing the lateral misfocus for the R and V bandpass images.

As a result, recovery of three bandpass images having different spatial-frequency content allows the generation of an SA with a cut-off frequency higher than the conventional one (NA of the microscope lens). Or equivalently, the SA generation implies a superresolved image by digitally computing the Fourier transform of the information contained in the SA. Such a superresolved image contains visible details that are not resolved in the low-resolution conventional image.

Thinking in terms of SA generation, Fig. 2 depicts how SESRIM approach defines an expanded cut-off frequency at the Fourier domain. The resolution limit (ρ) and the cut-off frequency (ν) are functions of the illumination wavelength

$$\rho = k \frac{\lambda}{\text{NA}} \Rightarrow \nu = \frac{1}{\rho} = \frac{\text{NA}}{k\lambda}, \quad (1)$$

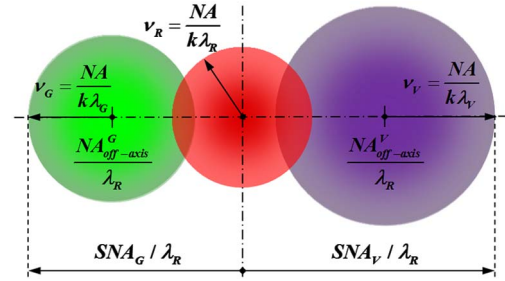


Fig. 2. (Color online) SA generation and expanded cut-off frequency definition by SESRIM.

where λ can be λ_R , λ_G , or λ_V and NA is the numerical aperture of the microscope lens. Because the NA of the lens is the same for all the wavelengths, the resolution limit and the cut-off frequency for the G and V beams can be expressed from the R wavelength values as

$$\rho_m = \rho_R \frac{\lambda_m}{\lambda_R} \Rightarrow \nu_m = \frac{\lambda_R}{\lambda_m} \nu_R, \quad (2)$$

where “ m ” can be G or V. And finally, as can be seen from Fig. 2, the cut-off frequency for the expanded aperture (ν_{SA}) in a given direction is obtained as the addition of the spatial frequency generated by the tilted beam illumination ($\nu_{\text{off-axis}}^m$) and the cut-off frequency for the specific wavelength of that tilted beam (ν_m):

$$\nu_{\text{SA}}^m = \nu_{\text{off-axis}}^m + \nu_m = \frac{\sin \theta_m}{\lambda_m} + \frac{\lambda_R}{\lambda_m} \nu_R. \quad (3)$$

By analogy, we can define a value for the off-axis NA of the tilted illumination beam as $\text{NA}_{\text{off-axis}}^m = \frac{\lambda_R}{\lambda_m} \sin \theta_m$, where the ratio $\frac{\lambda_R}{\lambda_m}$ appears as a consequence of referencing to the R wavelength. This value is not interpreted as a real NA value, because it is not representative of a full cone of light but as the direction provided by the outer and tilted ray of that cone of light. Now, according to Eq. (1), the cut-off frequency of the expanded SA (ν_{SA}) can be expressed as a function of the SNA:

$$\nu_{\text{SA}}^m = \frac{\text{SNA}_m}{\lambda_R} \Rightarrow \text{SNA}_m = \frac{\lambda_R}{\lambda_m} \left(\sin \theta_m + \frac{\text{NA}}{k} \right). \quad (4)$$

And finally, the value of the SNA defines a new resolution limit that we name as superresolution limit (ρ') in the form of

$$\rho'_m = \frac{\lambda_R}{\text{SNA}_m} \Rightarrow \rho'_m = \frac{\lambda_m}{\sin \theta_m + \frac{\text{NA}}{k}}. \quad (5)$$

For the two considered cases in this manuscript of 2D SESRIM extension, the generated SAs are depicted in Fig. 3. On the one hand, SESRIM with time multiplexing [Fig. 3(a)] allows full coverage of the 2D spatial-frequency domain but prevents the study of fast dynamics events. The input object is rotated to cover additional directions at the Fourier space. Here we have considered a rotation of 90° to cover the orthogonal (vertical) direction. On the other hand, SESRIM with selective angular multiplexing [Fig. 3(b)] allows a 2D single-exposure working principle but is restricted to real samples (objects with Hermitian spectral distribution) because only

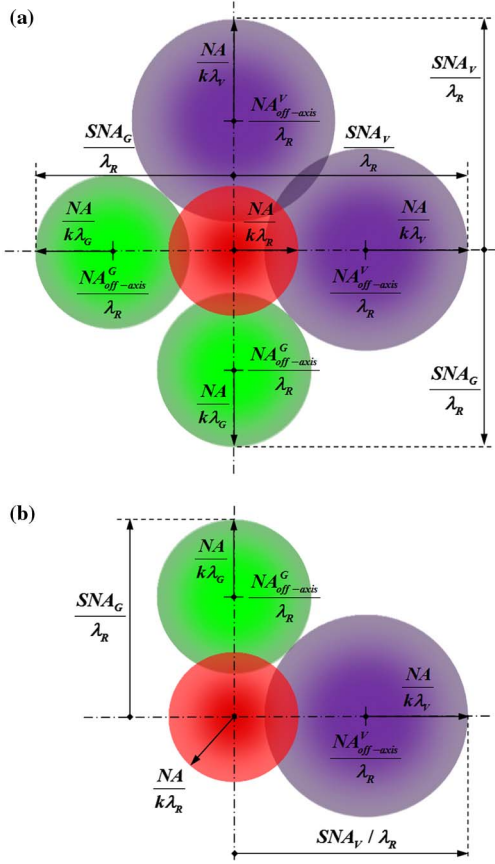


Fig. 3. (Color online) SA generation and expanded cut-off frequency for 2D SESRIM extension using (a) time multiplexing and (b) selective angular multiplexing.

one lateral pupil is recovered for each one of the two multiplexed directions.

Nevertheless, whatever the analyzed SESRIM setup will be and in its basic configuration, the generation of the SA comes from the coherent addition of three elementary pupils: one centered and two shifted apertures corresponding with the on-axis (R wavelength) and the two off-axis (G and V wavelengths) illumination beams, respectively. This process is digitally performed and involves the correct repositioning of the off-axis pupils in its original position at the object's spectrum, that is, to shift back at the Fourier domain those spatial frequencies of the object's spectrum that are downshifted by the angular multiplexing. Because the expanded cut-off frequency is essentially defined by the NA of each tilted illumination beam ($NA_{\text{off-axis}}^m$), we can choose between two different strategies when shaping the SA.

The first strategy implies that the off-axis illumination angle provided by the tilted beams will be exactly the angle defined by twice the NA of the used microscope lens. In this case, the recovered off-axis apertures will be contiguous with the central one at the Fourier domain [15,20,21,24,27], and SA generation must be guided by a visual criterion based on image quality improvement [30,31]. The second strategy deals with any other case where the off-axis pupils will not be contiguous with the central one. Here, the expanded SA could continuously cover the Fourier domain from the center by adding elementary apertures with overlapping regions [17,19,22,23,25]

or could not [18,28]. The case of partial overlapping between recovered pupils is quite common for a simple reason: it allows the use of digital computational tools based on correlation algorithms in the Fourier domain [29] or in the spatial domain [35] in order to optimize the assembly of the recovered elementary apertures. The former strategy maximizes the expanded cut-off frequency but prevents the use of digital methods based on the optimization of a given parameter (correlation peak) to properly replace each aperture. And the latter strategy allows a digital algorithm based on the correlation operation between overlapping areas to replace each elementary aperture with subpixel accuracy, but it reduces the cut-off frequency value of the expanded SA.

As in Ref. [34], in this manuscript we have adopted the algorithm reported by Bühl *et al.* to perform the reallocation of each elementary pupil [29]. Then, a given spectral area overlaps between the off-axis apertures (G and V pupils) with the central aperture (R pupil) when generating the SA. Moreover, because diffraction is wavelength dependent, the size of the elementary pupil increases as the wavelength decreases, providing an improvement in the overlapping spectral area. This fact improves the cut-off frequency of the SA while permitting the application of correlation methods to calculate the spatial-frequency shift for each aperture.

B. Mathematical SESRIM Analysis

Let us consider again the setup shown in Fig. 1. In the imaging arm, three different coplanar parallel RGV laser beams simultaneously illuminate the input plane but with different angles. Assuming the same incident amplitude “A” for all the beams, the illumination stage is mathematically represented by A , $A \cdot \exp(j2\pi\beta_G x)$ and $A \cdot \exp(j2\pi\beta_V x)$ corresponding with the RGV beams and where $\beta_G = \sin \theta_G / \lambda_G$ and $\beta_V = \sin \theta_V / \lambda_V$. Let us assume without lack of generality a 1D analysis of the system. Thus, the amplitude distribution of the input object is represented by $O(x)$, which is spatially limited by a slit of width “L” in the form of $\text{rect}(x/L)$. For the sake of simplicity, we present the calculations for a generic wavelength (λ) and for a generic tilted beam illumination in the form of $A \cdot \exp(j2\pi\alpha x)$, where λ and α can be $(\lambda_R, \lambda_G, \lambda_V)$ and $(0, \beta_G, \beta_V)$ for the RGV beams, respectively. Later on, we will finally generalize the result at the end of calculations because the three beams are incoherent one to each other.

Under these assumptions, the object is placed at a distance “d” in front of the microscope lens having a given focal length “f.” Because the RGV beams are collimated, the Fourier plane coincides with the back focal plane of the lens. The amplitude distribution $U(x_F)$ at the Fourier plane can be written as the Fourier transform of the input's plane distribution evaluated at the spatial frequency $u = x_F / \lambda f$; that is,

$$\begin{aligned}
 U(x_F) &= C \exp \left[j \frac{k}{2f} \left(1 - \frac{d}{f} \right) x_F^2 \right] \int O(x) \text{rect} \left(\frac{x}{L} \right) \\
 &\quad \times \exp(j2\pi\alpha x) \exp \left(-j \frac{2\pi}{\lambda f} x x_F \right) dx \\
 &= C \exp \left[j \frac{k}{2f} \left(1 - \frac{d}{f} \right) x_F^2 \right] \left[\tilde{O} \left(\frac{x_F}{\lambda f} - \alpha \right) \right. \\
 &\quad \left. \otimes L \text{sinc} \left(L \frac{x_F}{\lambda f} \right) \right], \tag{6}
 \end{aligned}$$

where \otimes represents convolution operation and $C = \frac{A \exp(jkf)}{j\lambda\sqrt{f}}$.

We can see how the spatial-frequency content of the input object is distributed around the position of the zero spatial frequency centered at $\lambda f \alpha$, as it corresponds with the generic tilted beam illumination.

Just behind the Fourier plane, the distribution provided by Eq. (6) is multiplied by $\text{rect}(x_F/x_{F0})$, representing the 1D pupil of the microscope lens placed on that plane and having a width of x_{F0} . This aperture restricts the range of spatial frequencies that can be transmitted by the objective, thus affecting the resolution. However, owing to the tilted beam illumination, the spatial-frequency content passing through the lens pupil is different for each wavelength. Naming \tilde{O}_R , \tilde{O}_G , and \tilde{O}_V as the spectral bandpasses of the object for the RGV wavelengths, respectively, the spatial-frequency content due to each illumination wavelength is restricted to

$$\begin{aligned} -\frac{x_{F0}}{2} \leq \lambda_R f u \leq \frac{x_{F0}}{2} &\Rightarrow -\frac{x_{F0}}{2\lambda_R f} \leq u \leq \frac{x_{F0}}{2\lambda_R f}, \\ -\frac{x_{F0}}{2} - \lambda_G f \beta_G \leq \lambda_G f u \leq \frac{x_{F0}}{2} - \lambda_G f \beta_G &\Rightarrow -\frac{x_{F0}}{2\lambda_G f} - \beta_G \leq u \leq \frac{x_{F0}}{2\lambda_G f} - \beta_G, \\ -\frac{x_{F0}}{2} - \lambda_V f \beta_V \leq \lambda_V f u \leq \frac{x_{F0}}{2} - \lambda_V f \beta_V &\Rightarrow -\frac{x_{F0}}{2\lambda_V f} - \beta_V \leq u \leq \frac{x_{F0}}{2\lambda_V f} - \beta_V, \end{aligned} \quad (7)$$

where the zero spatial frequency of the object's spectrum is located at " $\lambda_G f \beta_G$ " and " $\lambda_V f \beta_V$ " for the G and V wavelengths, respectively, as a consequence of the tilted beam illumination. By comparing Eq. (7) with Eqs. (1) and (2), we can establish the values of the system's cut-off frequencies for the three RGV considered wavelengths and disregarding the shift incoming from the tilted beam illumination (β_G, β_V):

$$\nu_R = \pm \frac{x_{F0}}{2\lambda_R f} \quad \text{and} \quad \nu_m = \pm \frac{\lambda_R}{\lambda_m} \nu_R = \pm \frac{\lambda_R}{\lambda_m} \frac{x_{F0}}{2\lambda_R f} = \pm \frac{x_{F0}}{2\lambda_m f}. \quad (8)$$

In order to get the three color-coded bandpass images O_R , O_G , and O_V provided by the microscope lens and incoming from \tilde{O}_R , \tilde{O}_G , and \tilde{O}_V , respectively, we must propagate Eq. (6) to the image plane (x_i, y_i) located at a distance " $d' - f$ " from the microscope lens and where the distances d and d' verify the lens law: $1/d + 1/d' = 1/f$. But before that, we must realize the fact that the three bandpass images will overlap one another at the image plane because they are transmitted in the on-axis mode. The three overlapping bandpass images can be captured and numerically processed in a single shot using RGB multiplexing when the detector is a color CCD camera [34]. But if the detector is a B&W CCD camera, we need to obtain the images spatially separated side by side with the additional constraint imposed by the limited detector's sensitive area. We get this image-plane spatial separation accomplished by inserting a 1D diffraction grating having an appropriate basic frequency (u_0) and looking at either the +1 or -1 diffraction order for getting the wavelength dispersion of the three color-coded bandpass images. Although the 1D grating is placed at the image space for the experiments, we assume here that the grating is placed just at the Fourier plane for simplifying the mathematical analysis with no loss of generality. Then, the amplitude transmittance of a sinusoidal grating can be written as

$$t(x_F) = \frac{1}{2} + \frac{m}{4} \exp(j2\pi u_0 x_F) + \frac{m}{4} \exp(-j2\pi u_0 x_F), \quad (9)$$

where m is the peak-to-peak change of amplitude transmittance. We will only pay attention to the second term because it is representative of the +1 diffraction order. Thus, the complete amplitude distribution $U'(x_F)$ at the Fourier plane comes from the inclusion in Eq. (6) of both the lens pupil function and the second term in Eq. (9):

$$\begin{aligned} U'(x_F) = C' \exp \left[j \frac{k}{2f} \left(1 - \frac{d}{f} \right) x_F^2 \right] &\left[\tilde{O} \left(\frac{x_F}{\lambda f} - \alpha \right) \right. \\ &\left. \otimes \text{Lsinc} \left(L \frac{x_F}{\lambda f} \right) \right] \text{rect} \left(\frac{x_F}{x_{F0}} \right) \exp(j2\pi u_0 x_F), \end{aligned} \quad (10)$$

with $C' = C \frac{m}{4}$. After propagating the distance " $d' - f$," the amplitude distribution in the output plane evaluated at the spatial frequency $u' = x_i/\lambda(d' - f)$ results in

$$\begin{aligned} U(x_i) = D \exp \left[j \frac{k}{2(d' - f)} x_i^2 \right] &\left\{ \text{FT} \left[\tilde{O} \left(\frac{x_F}{\lambda f} - \alpha \right) \right] \right. \\ &\left. \times \text{FT} \left[\text{Lsinc} \left(L \frac{x_F}{\lambda f} \right) \right] \right\} \\ &\otimes \text{FT} \left[\text{rect} \left(\frac{x_F}{x_{F0}} \right) \right] \otimes \text{FT}[\exp(j2\pi u_0 x_F)], \end{aligned} \quad (11)$$

where $D = \frac{m\lambda \exp(jkd')}{4f^2 \lambda^2 \sqrt{f(d' - f)}}$. Taking into account that

$$\begin{aligned} \text{FT} \left[\tilde{O} \left(\frac{x_F}{\lambda f} - \alpha \right) \right] &= \lambda f O \left(-\frac{x_i}{M} \right) \cdot \exp \left(j2\pi \frac{x_i}{M} \alpha \right), \\ \text{FT} \left[\text{Lsinc} \left(L \frac{x_F}{\lambda f} \right) \right] &= \lambda f \cdot \text{rect} \left(\frac{x_i}{ML} \right), \\ \text{FT} \left[\text{rect} \left(\frac{x_F}{x_{F0}} \right) \right] &= x_{F0} \cdot \text{sinc} \left(\frac{x_{F0} x_i}{\lambda f M} \right), \\ \text{FT}[\exp(j2\pi u_0 x_F)] &= \lambda f \cdot \delta \left(-\frac{x_i}{M} - \lambda f u_0 \right), \end{aligned} \quad (12)$$

where the magnification M is given by $M = -\frac{d' - f}{f}$, the final result concerning the amplitude distribution arriving at the CCD from the imaging branch can be written as

$$\begin{aligned} U(x_i) = D' \exp \left[j \frac{k}{2(d' - f)} x_i^2 \right] &\times \left\{ O \left(-\frac{x_i}{M} \right) \exp \left(j2\pi \frac{x_i}{M} \alpha \right) \text{rect} \left(\frac{x_i}{ML} \right) \right\} \\ &\otimes \text{sinc} \left(\frac{x_{F0} x_i}{\lambda f M} \right) \otimes \delta \left(-\frac{x_i}{M} - \lambda f u_0 \right), \end{aligned} \quad (13)$$

where $D' = D \lambda^3 f^3 x_{F0}$. Equation (13) shows, first, and it was expected, a smoothing effect on the color-coded bandpass image of the object due to the convolution with the sinc function (incoming from the Fourier transform of the lens pupil) and, second, that the position of the bandpass image is dependent on the wavelength for fixed the values of M, f , and u_0 (incoming from the convolution with the delta function). When considering the three color-coded bandpass images, they will be placed at different spatial positions at the image plane. And the width of each bandpass image will be given by the addition of both the rectangle function width (ML) and the sinc

function width (taken as the distance between the two zeros of the central lobe: $2\lambda fM/x_{F0}$). Moreover, the R bandpass image is shifted more than the G image, which is also shifted more than the V image. And taking into account that the three color-coded bandpass images must be fitted inside the CCD sensitive area, we can look for the condition to avoid the overlapping of the different bandpass images. To assure that the V image is separated from the G image, the spatial position of the upper frequency of the V image must be equal to or smaller than the lowest frequency of the G image; that is,

$$\lambda_V f u_0 + \frac{1}{2}LM + \frac{\lambda_V f M}{x_{F0}} \leq \lambda_G f u_0 - \frac{1}{2}LM - \frac{\lambda_G f M}{x_{F0}} \Rightarrow u_0 \geq \frac{M}{x_{F0}} \left(\frac{\lambda_G + \lambda_V}{\lambda_G - \lambda_V} \right) + \frac{ML}{f(\lambda_G - \lambda_V)}. \quad (14)$$

In a similar way, we can obtain the condition to be fulfilled between R and G bandpass images to avoid overlapping

$$\lambda_G f u_0 + \frac{1}{2}LM + \frac{\lambda_G f M}{x_{F0}} \leq \lambda_R f u_0 - \frac{1}{2}LM - \frac{\lambda_R f M}{x_{F0}} \Rightarrow u_0 \geq \frac{M}{x_{F0}} \left(\frac{\lambda_R + \lambda_G}{\lambda_R - \lambda_G} \right) + \frac{ML}{f(\lambda_R - \lambda_G)}. \quad (15)$$

Then, from Eqs. (14) and (15) we choose the highest value of u_0 that will preserve the spatial separation of the three color-coded bandpass images because the lower one will provide separation between the G and V bandpass images but overlapping between the R and G images.

Under these conditions, the B&W CCD camera simultaneously records the three color-coded bandpass images, each of them containing a different spatial-frequency range that are placed side by side without overlapping. In order to preserve the information of the amplitude and phase of each bandpass image, a holographic recording is performed by inserting at the CCD plane three collinear reference beams arriving from the reference branch of the Mach-Zehnder interferometer (see Fig. 1). Those three reference beams diverge from the same distance “ $d' - f$ ” in front of the CCD in order to cancel the quadratic phase factor of the imaging beam [the term between square brackets in Eq. (13)]. The reference beam can be mathematically expressed as

$$R(x_i) = \exp\left(j2\pi \frac{\sin \varphi}{\lambda} x_i\right) \cdot \exp\left[j \frac{k}{2(d' - f)} x_i^2\right], \quad (16)$$

where φ is the angle between the propagation direction of a given bandpass image and the direction of the reference beam.

In addition, the reference mirror at the reference arm is tilted to allow off-axis holographic recording. Thus, the average direction of the three reference beams in addition to the slightly different propagation direction provided by dispersion in the +1 diffraction order of the 1D grating produce a slightly different carrier for each color-coded bandpass image. This fact means that we will have three slightly different carriers ($\sin \varphi_R/\lambda_R$, $\sin \varphi_G/\lambda_G$, $\sin \varphi_V/\lambda_V$) for the three subholograms incoming from the RGV wavelengths.

Finally, the CCD records the intensity distribution provided by the image-plane hologram and incoming from the addition of Eqs. (13) and (16). As is well known, such an intensity distribution has four contributions according to

$$I(x_i) = |U(x_i) + R(x_i)|^2 = |U(x_i)|^2 + |R(x_i)|^2 + U(x_i)R^*(x_i) + U^*(x_i)R(x_i), \quad (17)$$

and the term $U(x_i)R^*(x_i)$ that appears in the amplitude transmittance of the digitally recorded hologram contains information about the complex amplitude distribution of the three color-coded bandpass images. Then, the reconstruction process is performed numerically. Because of the slightly different carriers of the three subholograms, the three elementary apertures will not be as centered rectangles (concentric circular apertures when considering the 2D lens pupil) at the Fourier domain. But in any case, those apertures are filtered aside from both the zero order and the twin image term and inversely Fourier transformed to obtain the complex amplitude distribution of the three bandpass images provided by the three RGV beams. The digital combination of the information contained in the three color-coded bandpass images yields in the SA generation we are looking for, as was explained in Subsection 2.A.

3. EXPERIMENTAL IMPLEMENTATIONS

The experimental setup presented in Subsection 2.A has been assembled at the laboratory. Three laser sources provide the three simultaneous illumination wavelengths: an He-Ne red (R) laser source (632.8 nm laser wavelength, 35 mW optical power), a green (G) diode-pumped laser module (532 nm laser wavelength, 50 mW optical power), and a violet (V) laser diode module (405 nm laser wavelength, 50 mW optical power). Prior to illuminating the input object (a negative USAF resolution test target), a reference beam is extracted for each one of the illumination beams in order to allow holographic image-plane recording. A 1D slit (140 μm width, chrome on glass with a clear slit and chrome background) is placed face to face with the input object to provide object FOV limitation. This input plane amplitude distribution is imaged by a long-working-distance infinity-corrected microscope lens (Mitutoyo M Plan Apo 0.14 NA) onto a monochrome CCD camera (Kappa DC2, 12 bits, 1352×1032 pixels with 6.7 μm pixel size). But prior to that, a high-precision Ronchi ruling grating (50 lp/mm) is used to provide wavelength dispersion of the three bandpass images at the image space when looking at one of the first diffraction orders of the grating. In the reference arm, a 5 \times beam expander and a doublet lens (80 mm focal length) provide the same beam divergence as the imaging beam. Additional neutral density filters allow laser beam power equalization and improve fringe contrast in the holographic recording.

A. SESRIM by Image-Plane Wavelength-Dispersion Multiplexing

In this first subsection, we present the validation of SESRIM using wavelength dispersion at the image plane to angularly separate the three transmitted bandpass images. Figure 4 shows the experimental results where the coplanar but opposite tilted illumination angles for the G and V beams are $\theta_G = 13.5^\circ$ and $\theta_V = 12^\circ$, respectively. The recorded hologram produced by the addition of the three bandpass images with the three reference beams is depicted in Fig. 4(a), while its Fourier transform is presented in Fig. 4(b). Because of wavelength coding, each bandpass image arrives at the CCD plane with a slightly different incident angle after being dispersed by the 1D diffraction grating. As a consequence, each one of the

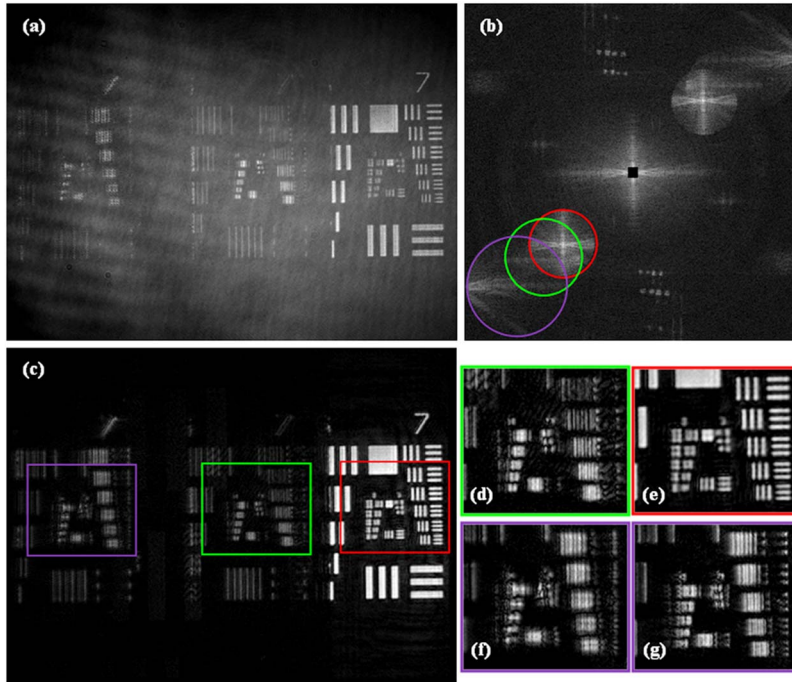


Fig. 4. (Color online) Experimental results for SESRIM in the horizontal direction: (a) recorded hologram; (b) Fourier transform of (a); (c) recovered complex amplitude distribution image containing information of the three transmitted bandpass images; (d)–(e) magnification of the central part of the bandpass images corresponding with the green and red lasers, respectively; and (f)–(g) the same magnified area for the blue laser bandpass image showing the misfocused and refocused images, respectively.

three subholograms will have a slightly different carrier frequency. One can notice this fact because the three elementary apertures are not concentric circles at the Fourier domain [Fig. 4(b)].

Once the three elementary apertures are filtered aside from both the zero order and twin image terms and inversely Fourier transformed, a complex (amplitude and phase) image of the amplitude distribution arriving from the input plane is retrieved [Fig. 4(c)]. However, only the R bandpass image [red (rightmost) rectangle in Figs. 4(c) and 4(e)] is in focus due to the chromatic aberration of the microscope lens. Then, the G and V bandpass images are digitally refocused prior to their combining in the SA. Just as an example, Figs. 4(f) and 4(g) depict the misfocused and refocused central part of the V bandpass image, respectively.

After digital refocusing the G and V bandpass images, the SA is assembled by digital processing based on optimization of the correlation peak between overlapping areas of the recovered pupils, that is, between the G and R pupils on one hand, and between the V and R pupils on the other hand. The conventional aperture (only considering on-axis R laser illumination) and the conventional low-resolution image are presented in Figs. 5(a)–5(c). Paying attention to Fig. 5(c), the last resolved element is Group 8—Element 1 (hereafter called Gx-Ey), which corresponds with the features size of $3.9\ \mu\text{m}$ (or 256 lp/mm). From this resolution limit, we can calculate the value of the proportional constant k as $k = \rho_R \text{NA} / \lambda_R = 0.86$. This k value is in good agreement with the one ($k = 0.82$) reported in Refs. [2,3].

Finally, a superresolved image is obtained as an inverse Fourier transform of the information contained in the SA [Fig. 5(b)]. We can see that the resolution limit is improved from G8-E1 to the last resolution test element (G9-E3) for the superresolved image [Fig. 5(d)]. Quantitatively, this fact

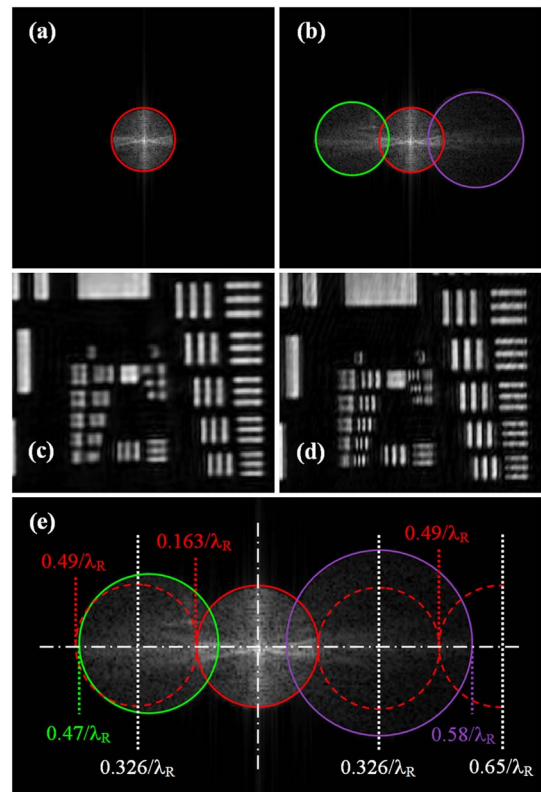


Fig. 5. (Color online) Experimental results for SESRIM in the horizontal direction: (a), (b) comparison between conventional and expanded apertures, respectively; (c), (d) conventional (low-resolution) and superresolved images, respectively; and (e) schematic composition between the generated SA (case b) and the theoretical values of spatial frequencies expressed as a ratio between the NA (or SNA) and the R wavelength.

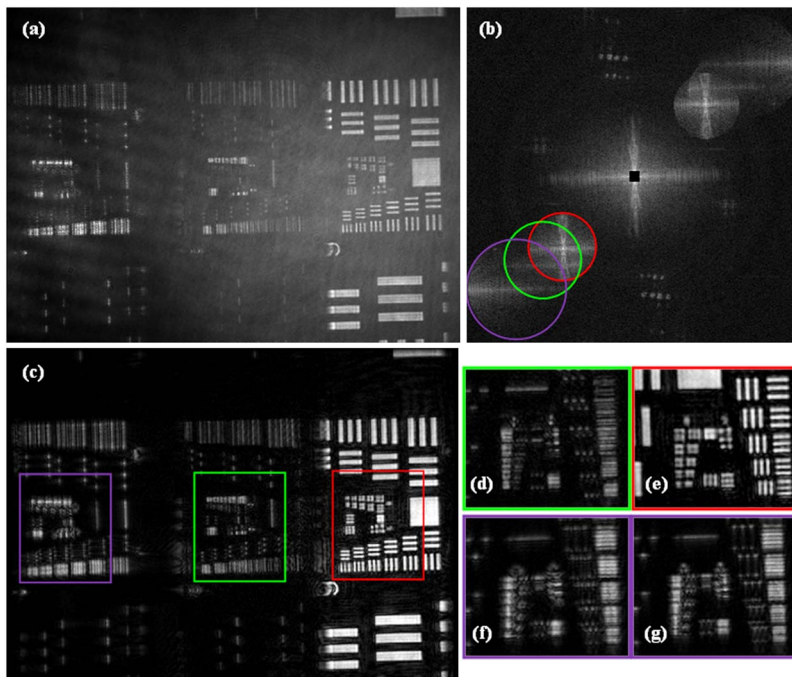


Fig. 6. (Color online) Experimental results for SESRIM in the vertical direction: (a) recorded hologram, (b) Fourier transform of (a); (c) recovered complex amplitude distribution image containing information of the three transmitted bandpass images; (d), (e) magnified and rotated image of the central part of the bandpass images corresponding with the green and red lasers, respectively; and (f), (g) the same magnified and rotated area for the blue laser bandpass image showing the misfocused and refocused images, respectively.

means that the resolution limit is improved from $3.91\ \mu\text{m}$ (256 lp/mm) to $1.55\ \mu\text{m}$ (645 lp/mm), defining an experimental resolution gain factor of approximately 2.5.

When compared with theory, the resolution limit of the superresolved image is indeed better. According to Eqs. (4) and (5) and using $k = 0.86$, the SNA and the superresolution limits for both multiplexed directions are $\text{SNA}_G = 0.47$ and $\rho'_G = 1.35\ \mu\text{m}$ for the G wavelength and $\text{SNA}_V = 0.58$ and $\rho'_V = 1.09\ \mu\text{m}$ for the V wavelength. Both superresolution limits are below the minimum pitch included in the test (G9-E3 corresponding with $1.55\ \mu\text{m}$), and the theoretical resolution gain factors are approximately 2.9 and 3.6, for the G and V cases, respectively. To validate those theoretical values, we have included in Fig. 5(e) a virtual composition between the generated SA [Fig. 5(b)] and the theoretical values of the spatial frequencies expressed as a ratio between NA (or SNA) and the R wavelength to easily identify the values. Considering the V multiplexed direction, we can see that the center of the V aperture ($\text{NA}_{\text{off-axis}}^V = \frac{\lambda_R}{\lambda_V} \sin \theta_V = 0.325 \Rightarrow \nu_{\text{off-axis}}^V = \frac{0.325}{\lambda_R}$) almost coincides with the center of a hypothetical R pupil (dashed red inner circle) placed contiguously with the conventional aperture (solid red inner circle). The right side of such a contiguous R aperture corresponds with a cut-off frequency of $0.49/\lambda_R$ and defines a NA gain factor of 3 and, thus, also the same improvement in resolution. An additional contiguous R aperture will be centered at $0.65/\lambda_R$ defining a gain factor of 4, and the right side of the V aperture ($\nu_{\text{SA}}^V = 0.58/\lambda_R$) is near the middle of $0.49/\lambda_R$ and $0.65/\lambda_R$ but a little bit closer to $0.65/\lambda_R$, thus defining a resolution gain factor of 3.6. For the G case, the left side of the G pupil ($\nu_{\text{SA}}^G = 0.47/\lambda_R$) nearly triples the cut-off frequency when considering the conventional R aperture. So, the gain factor is close to 3.

B. Extension to the 2D Case Considering Time Multiplexing in SESRIM

The most direct way to perform a 2D extension of SESRIM is by rotating the object at the input plane to perform angular multiplexing provided by the illumination stage in additional Fourier domain directions. As was also reported in Ref. [34], Fig. 6 shows the experimental results when the USAF test is rotated 90° and SESRIM is again implemented. Note that the object's rotation provides the same effect as a rotation in the illumination plane but in a simpler way. Once again, the tilted

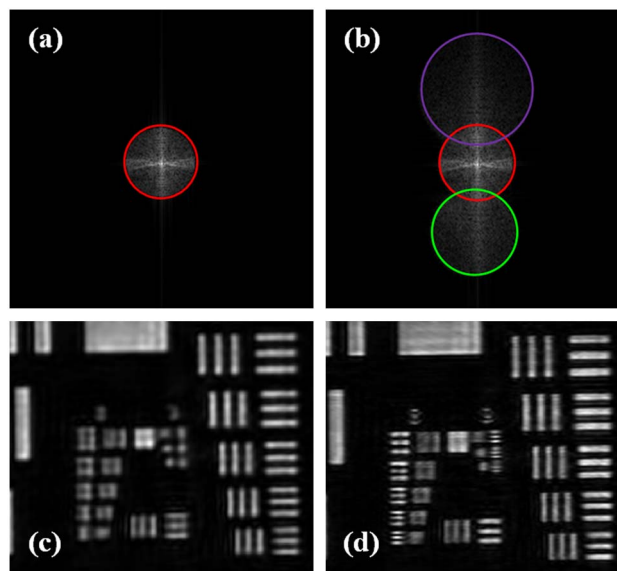


Fig. 7. (Color online) Experimental results for SESRIM in the vertical direction: (a)–(b) comparison between conventional and expanded apertures, respectively, and (c)–(d) conventional (low-resolution) and superresolved images, respectively.

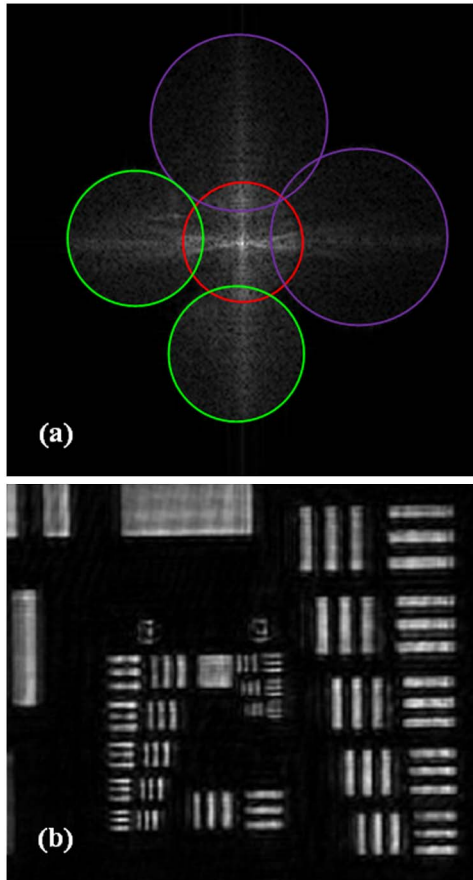


Fig. 8. (Color online) 2D extension of SESRIM considering time multiplexing: (a) generated SA and (b) 2D superresolved image.

illumination angles for the G and V beams are the same as in the previous experiment. Figure 6(a) depicts the recorded hologram being produced. Figure 6(b) shows the Fourier transform of Fig. 6(a). Figure 6(c) shows the complex amplitude distribution image recovered after the filtering process performed in Fig. 6(b). Figures 6(d)–6(g) depict the bandpass images of the USAF central part for the different wavelengths, showing as an example the misfocus and refocus of the V bandpass image [cases (f) and (g)].

The SNA and superresolution values are the same as in the previous subsection but in the orthogonal direction. Figures 7(a) and 7(b) depict the conventional and generated

SA, respectively, while the conventional and 1D superresolved image is presented in Figs. 7(c) and 7(d), respectively. But now, the expanded SAs shown in Figs. 5(b) and 7(b) are combined to synthesize a 2D SA containing information in both multiplexed directions. The result is presented in Fig. 8(a) showing an SA composed by the coherent addition of four off-axis (two horizontal and two vertical) apertures plus the on-axis aperture. Thus, the superresolved image [Fig. 8(b)] contains information on both multiplexed directions.

C. Extension to the Two-Dimensional Case Considering Selective Angular Multiplexing in SESRIM

As a second way to obtain 2D SESRIM, we report on the possibility to multiplex orthogonal directions of the object's spectrum by the two tilted beams used in the illumination stage. Thus, the G wavelength provides the recovery of an elementary aperture with spectral information in the vertical diffraction direction, while the V wavelength allows simultaneous recovery of the spatial-frequency information in the horizontal diffraction direction. This selective angular multiplexing in SESRIM permits a 2D superresolved image in a single exposure. Nevertheless, because only three recovered apertures are available by SESRIM, only one side of the object's spectrum for any of the two multiplexed directions is recovered. This means that this method is useful for synthetic objects without relevant phase information, that is, only quasi-real objects having a Hermitian Fourier transform are susceptible to imaging with 2D SESRIM with selective angular multiplexing.

To validate this modification of SESRIM, we have slightly modified the experimental setup depicted in Fig. 1 to include vertical off-axis illumination for the G wavelength. Thus, two mirrors bend the G laser beam into the vertical plane allowing an off-axis illumination angle of approximately 13° . The rest of the experimental setup has no additional modifications regarding the description included in Subsection 3.A. The experimental assembly is presented in Fig. 9(a), showing a picture from the upper view including the ray tracing of the three laser beams, while Fig. 9(b) shows a picture of the illumination stage [white rectangle in Fig. 9(a)] to clearly show the selective angular multiplexing. In addition, one can identify the 1D slit limiting the FOV at the input plane in Fig. 9(b).

Figure 10 presents the experimental results: (a) images the recorded hologram composed by three bandpass images, (b) depicts the Fourier transform of the recorded hologram, (c) shows the complex amplitude distribution image

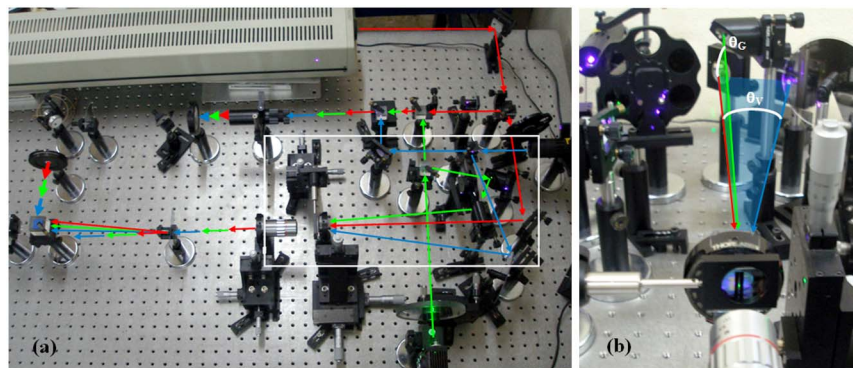


Fig. 9. (Color online) Experimental arrangement of SESRIM with selective angular multiplexing: (a) full experimental implementation with ray tracing and (b) detail of the selective angular illumination procedure [picture corresponding with the white rectangle in (a)].

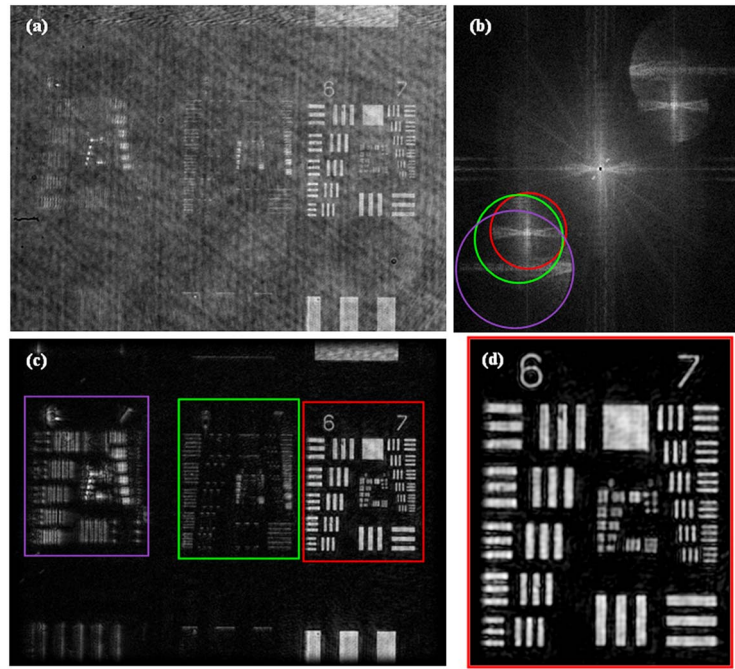


Fig. 10. (Color online) Experimental results for 2D SESRIM using selective angular multiplexing: (a) recorded hologram, (b) Fourier transform of (a), (c) recovered complex amplitude distribution image containing information of the three transmitted bandpass images, and (d) conventional (low-resolution) image provided by the red laser bandpass image.

recovered after filtering the diffraction orders in (b), and (d) presents the conventional low-resolution image obtained when only on-axis R illumination is used. And finally, Fig. 11 shows the experimental results concerning (a) the generated SA and (b) the superresolved image. Because the off-axis illumination angle for the G wavelength ($\theta_G = 13^\circ$) is a little bit smaller than in the previous experiments ($\theta_G = 13.5^\circ$), the theoretical values are slightly different ($\text{SNA}_G = 0.46$, $\rho'_G = 1.38 \mu\text{m}$, resolution gain factor of 2.8) but, in any case, enough to resolve the small details of the USAF test target. Obviously, the V multiplexed direction remains unchanged and with the same theoretical values.

We want to emphasize that 2D SESRIM by selective angular multiplexing does not restrict the object FOV as much as 2D SESRIM by time multiplexing. As we can see from the generated superresolved images in both cases [Figs. 8(b) and 11(b)], the allowed FOV when rotating the object is limited to a square area having a side equal to the width of the 1D slit used to limit the FOV. Now, with selective angular multiplexing, the FOV of the superresolved image is expanded in the direction of the 1D slit.

D. Avoiding the Field-of-View Limitation in SESRIM with a Monochrome Sensor

In order to completely remove the FOV restriction imposed by SESRIM, we present a further implementation where instead of recovering the complex amplitude distribution of the three bandpass images by separating them via spatial multiplexing at the output plane, the separation is performed at the Fourier plane. Thus, the 1D slit and the 1D dispersive grating are not needed anymore, which yields a full FOV superresolved image. To accomplish the recovery of the bandpass images, the angle of incidence of the three reference beams must be slightly varied between them. As a consequence, each subhologram

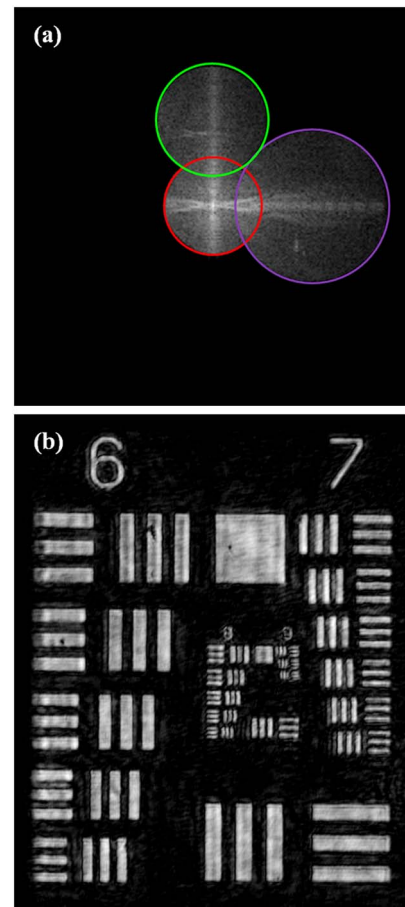


Fig. 11. (Color online) 2D extension of SESRIM considering selective angular multiplexing: (a) generated SA and (b) 2D superresolved image.

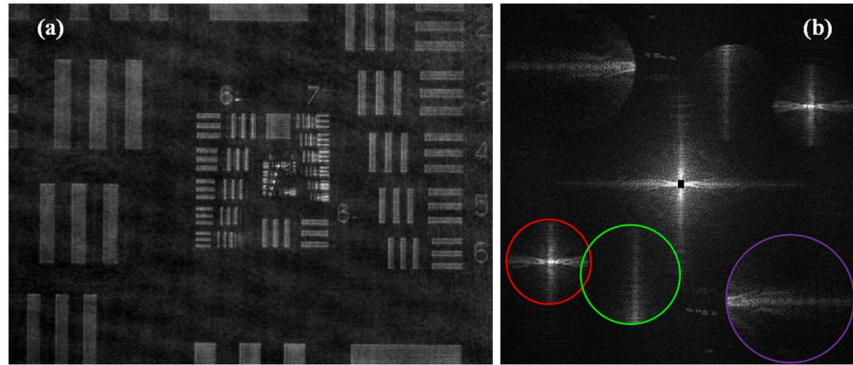


Fig. 12. (Color online) Experimental results for 2D SESRIM by avoiding the FOV limitation: (a), (b) the recorded hologram and its Fourier transform, respectively, where the DC term has been blocked down to enhance image contrast.

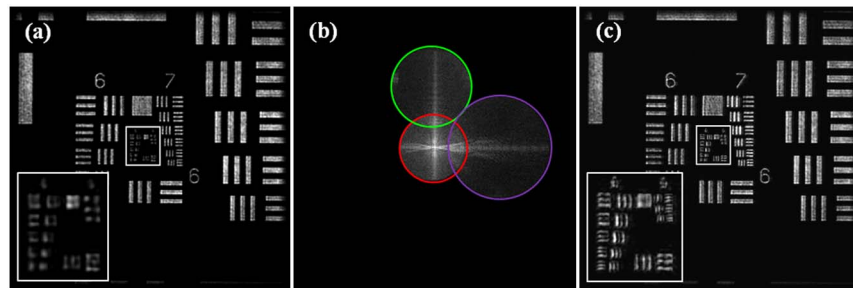


Fig. 13. (Color online) SESRIM without considering FOV restriction: (a) low-resolution conventional image, (b) generated SA, and (c) 2D superresolved image. Insets in (a) and (c), USAF central part magnified for clarity.

provides a different carrier frequency allowing the separation of the elementary apertures in the Fourier domain.

The experimental configuration is the same one as previously reported in Subsection 3.C, and it includes inserting a 1D diffraction grating in the reference arm to produce a variation in the propagation angle of each reference beam. Thus, taking into account the first diffraction order of the grating, each reference beam is diffracted at a different angle according to its wavelength and the grating's period (400 lp/mm). Figure 12 depicts (a) the recorded hologram composed by the addition of the three subholograms but without the 1D slit used in previous subsections for FOV limitation and (b) the Fourier transform of the recorded hologram showing that the three elementary apertures are dispersed at the Fourier domain. Note that the FOV presented in Fig. 12(a) is wider than the one included in, for instance, Figs. 4(a) and 10(a).

The selection of the grating's period is experimentally adjusted according to the pupil separation at the Fourier domain. As we can see from Fig. 12(b), the apertures for the R and V wavelengths must be at the borders of the spatial-frequency space in order to satisfy Nyquist sampling criterion allowing the maximum separation between apertures. However, the R and G apertures partially overlap as a consequence of reducing the wavelengths' step between the G and R wavelengths (101 nm) in comparison to the step between the G and V wavelengths (127 nm). This fact could be avoided by using a different combination of laser wavelengths in which the wavelength step between the R, G, and V illuminations will be properly selected to avoid overlapping. Nevertheless, the overlapping between the R and G pupils causes some noise in the final reconstruction, but it is not relevant for the USAF test case because the most important information is in the vertical direction. Finally, Fig. 13 presents (a) the conventional

low-resolution image obtained when only on-axis R illumination is considered, (b) the generated SA where the R pupil intrusion appears at the left border of the G aperture, and (c) the 2D superresolved image.

4. CONCLUSIONS AND DISCUSSION

In this manuscript, we have presented a modification and its evolutions of our previously reported SESRIM concept [34]. Starting from a theoretical analysis of the SESRIM basics, the new layout replaces the color CCD camera, used in our previous publication, by a monochrome CCD. Thus, the resolution is not affected by a large effective pixel size when sampling the output image (as usually happens in color CCD with a Bayer filter), because the B&W CCD uses all the disposable pixels. This fact reduces the need to use high magnification ratios between the input and output planes to circumvent the large effective pixel size of the color CCD, and the obtained object FOV could be, in principle, larger than for the color CCD case. Because the monochrome sensor does not allow separate recovery of the three color-coded holograms, the single-exposure working principle is saved by using FOV limitation at the input plane using a 1D slit positioned in close contact with the input object and output plane space-division multiplexing provided by a 1D grating. Experimental results are provided and demonstrate a good match to the theoretical predictions.

Then, 2D extension of 1D SESRIM with a monochrome CCD is considered by two different methods: using time multiplexing and using selective angular multiplexing. The former allows full coverage of the 2D spatial-frequency domain by rotating the input object while preventing the study of fast dynamics events due to its underlying time multiplexing principle. And the latter allows a 2D single-exposure working

principle, but it is limited to real objects. Once again, experiments are reported validating both 2D SESRIM extensions.

And finally, a third SESRIM case is also included where the main advantage is the elimination of the object FOV restriction. The 1D slit is removed, and the complex amplitude distribution of the three bandpass images is recovered by a filtering process at the Fourier domain instead of spatial separation at the output plane. To achieve elementary aperture separation at the Fourier domain, the incidence angle of each reference beam varies from one to the others. Experimental validation has also been presented.

In summary, different combinations of different multiplexing domains have been reported to implement SESRIM with a monochrome sensor. Because the SESRIM illumination stage is based on both wavelength and angular multiplexing and the detector is not wavelength sensitive, additional multiplexing domains are needed to recover separately the information contained in each wavelength channel: reduction of the usable object FOV and spatial image-plane multiplexing. This is the case of the basic layout presented in Subsection 3.A. The 2D extension included in Subsection 3.B combines wavelength, angular, FOV, and spatial multiplexing with the temporal domain to cover additional directions at the Fourier domain. Subsection 3.C proposes a mixing of previous cases to avoid time multiplexing while allowing single-exposure 2D SESRIM by selective angular multiplexing, once again in addition with wavelength, FOV, and spatial multiplexed domains. And finally, Subsection 3.D presents the combination of the wavelength with angular but without FOV and spatial multiplexing domains. Here, the limitation is performed in the dynamic range of the CCD sensor. Future implementations of SESRIM could be aimed at combining the polarization with wavelength and angular multiplexing in the illumination stage in order to allow 2D SESRIM coverage of the full spatial-frequency domain.

There are three main drawbacks when applying the proposed method and depending on the experimental configuration. The first one concerns the loss of object color information provided by the proposed method. Because SESRIM uses wavelength multiplexing to decode the three transmitted bandpass images, the color object information is lost. For this reason, SESRIM is restricted to objects having no color information.

The second drawback is related to the FOV limitation imposed by those experiments where the bandpass images are recovered by image-plane spatial filtering (not present in the last experiment where the three reference beams are inserted with a different angle at the recording plane). Obviously, the FOV limitation restricts the maximum extension of the input object that can be imaged. But first, the FOV limitation is only in the horizontal direction (the direction where the spectral separation is provided by the 1D diffraction grating). And second, even in the horizontal direction, the resulting FOV is around $140\ \mu\text{m}$ due to the width of the 1D slit attached to the input object. This value is between the ones provided by the Mitutoyo M Plan Apo $20\times 0.42\ \text{NA}$ and $50\times 0.55\ \text{NA}$ objectives considering a $1/2\ \text{in.}$ sensor size, that is $320\times 240\ \mu\text{m}$, and $130\times 100\ \mu\text{m}$ according to theoretical specifications, respectively. Because the SNA achieved in the proposed approach is around 0.47, the FOV provided by our SESRIM approach is comparable in the horizontal direction to those values provided by equivalent NA microscope lenses, while

it becomes enlarged in the vertical direction where no slit limitation is introduced.

And finally, as a third drawback, we find the dynamic range limitation is imposed when recording the multiplexed hologram as a consequence of the addition of multiple reference beams in the recording. Considering the experiment where the FOV limitation is removed (note that this is the worst case because not only the reference beams but also the three bandpass images overlap at the image plane), we have the addition of three independent holograms (one to each RGB wavelength) at the CCD plane. Because we are using a 12 bits CCD, there are around 1365 gray levels accessible for each wavelength channel, meaning around $\log(4096/3)/\log(2) = 10.4\ \text{bits}$ in dynamic range per channel. This value is higher than the standard 8 bits range provided by commonly available CCD cameras. Moreover, thinking about the addition of two additional tilted beams to cover full 2D spatial-frequency range in the Fourier domain, that is, to obtain 2D SESRIM, the disposable dynamic range per hologram without reducing the FOV is $\log(4096/5)/\log(2) = 9.68\ \text{bits}$, still higher than the 8 bits conventional value.

REFERENCES

1. E. Abbe, "Beitrag zur Theorie des Mikroskops und der mikroskopischen Wahrnehmung," *Arch. Mikrosk. Anat.* **9**, 413–418 (1873).
2. M. Born and E. Wolf, *Principles of Optics*, 7th (expanded) ed. (Cambridge University, 1999).
3. Y. Cotte, M. F. Toy, E. Shaffer, N. Pavillon, and C. Depeursinge, "Sub-Rayleigh resolution by phase imaging," *Opt. Lett.* **35**, 2176–2178 (2010).
4. Z. Zalevsky and D. Mendlovic, *Optical Super Resolution* (Springer, 2002).
5. T. Zhang and I. Yamaguchi, "Three-dimensional microscopy with phase-shifting digital holography," *Opt. Lett.* **23**, 1221–1223 (1998).
6. E. Cuche, P. Marquet, and C. Depeursinge, "Simultaneous amplitude-contrast and quantitative phase-contrast microscopy by numerical reconstruction of Fresnel off-axis holograms," *Appl. Opt.* **38**, 6994–7001 (1999).
7. F. Dubois, L. Joannes, and J.-C. Legros, "Improved three-dimensional imaging with a digital holography microscope with a source of partial spatial coherence," *Appl. Opt.* **38**, 7085–7094 (1999).
8. T. Colomb, F. Dürr, E. Cuche, P. Marquet, H. G. Limberger, R. P. Salathé, and C. Depeursinge, "Polarization microscopy by use of digital holography: application to optical-fiber birefringence measurements," *Appl. Opt.* **44**, 4461–4469 (2005).
9. P. Ferraro, S. De Nicola, A. Finizio, G. Coppola, S. Grilli, C. Magro, and G. Pierattini, "Compensation of the inherent wave front curvature in digital holographic coherent microscopy for quantitative phase-contrast imaging," *Appl. Opt.* **42**, 1938–1946 (2003).
10. J. Sheng, E. Malkiel, and J. Katz, "Digital holographic microscopy for measuring three-dimensional particle distributions and motions," *Appl. Opt.* **45**, 3893–3901 (2006).
11. P. Ferraro, S. Grilli, D. Alfieri, S. De Nicola, A. Finizio, G. Pierattini, B. Javidi, G. Coppola, and V. Striano, "Extended focused image in microscopy by digital holography," *Opt. Express* **13**, 6738–6749 (2005).
12. P. Marquet, B. Rappaz, P. J. Magistretti, E. Cuche, Y. Emery, T. Colomb, and Ch. Depeursinge, "Digital holographic microscopy: a noninvasive contrast imaging technique allowing quantitative visualization of living cells with subwavelength axial accuracy," *Opt. Lett.* **30**, 468–470 (2005).
13. F. Dubois, C. Yourassowsky, O. Monnom, J.-C. Legros, O. Debeir, P. Van Ham, R. Kiss, and C. Decaestecker, "Digital holographic microscopy for the three-dimensional dynamic analysis of *in vitro* cancer cell migration," *J. Biomed. Opt.* **11**, 054032 (2006).

14. T. Sato, M. Ueda, and G. Yamagishi, "Superresolution microscope using electrical superposition of holograms," *Appl. Opt.* **13**, 406–408 (1974).
15. C. J. Schwarz, Y. Kuznetsova, and S. R. J. Brueck, "Imaging interferometric microscopy," *Opt. Lett.* **28**, 1424–1426 (2003).
16. V. Mico, Z. Zalevsky, P. García-Martínez, and J. García, "Single step superresolution by interferometric imaging," *Opt. Express* **12**, 2589–2596 (2004).
17. V. Mico, Z. Zalevsky, P. García-Martínez, and J. García, "Super-resolved imaging in digital holography by superposition of tilted wavefronts," *Appl. Opt.* **45**, 822–828 (2006).
18. S. A. Alexandrov, T. R. Hillman, T. Gutzler, and D. D. Sampson, "Synthetic aperture Fourier holographic optical microscopy," *Phys. Rev. Lett.* **97**, 168102 (2006).
19. V. Mico, Z. Zalevsky, and J. García, "Superresolution optical system by common-path interferometry," *Opt. Express* **14**, 5168–5177 (2006).
20. V. Mico, Z. Zalevsky, P. García-Martínez, and J. García, "Synthetic aperture superresolution using multiple off-axis holograms," *J. Opt. Soc. Am. A* **23**, 3162–3170 (2006).
21. Y. Kuznetsova, A. Neumann, and S. R. J. Brueck, "Imaging interferometric microscopy—approaching the linear systems limits of optical resolution," *Opt. Express* **15**, 6651–6663 (2007).
22. J. R. Price, P. R. Bingham, and C. E. Thomas, Jr., "Improving resolution in microscopic holography by computationally fusing multiple, obliquely illuminated object waves in the Fourier domain," *Appl. Opt.* **46**, 827–833 (2007).
23. G. Indebetouw, Y. Tada, J. Rosen, and G. Brooker, "Scanning holographic microscopy with resolution exceeding the Rayleigh limit of the objective by superposition of off-axis holograms," *Appl. Opt.* **46**, 993–1000 (2007).
24. V. Mico, Z. Zalevsky, and J. García, "Synthetic aperture microscopy using off-axis illumination and polarization coding," *Opt. Commun.* **276**, 209–217 (2007).
25. V. Mico, Z. Zalevsky, and J. García, "Common-path phase-shifting digital holographic microscopy: a way to quantitative phase imaging and superresolution," *Opt. Commun.* **281**, 4273–4281 (2008).
26. A. Neumann, Y. Kuznetsova, and S. R. Brueck, "Structured illumination for the extension of imaging interferometric microscopy," *Opt. Express* **16**, 6785–6793 (2008).
27. V. Mico, Z. Zalevsky, C. Ferreira, and J. García, "Superresolution digital holographic microscopy for three-dimensional samples," *Opt. Express* **16**, 19260–19270 (2008).
28. T. R. Hillman, T. Gutzler, S. A. Alexandrov, and D. D. Sampson, "High-resolution, wide-field object reconstruction with synthetic aperture Fourier holographic optical microscopy," *Opt. Express* **17**, 7873–7892 (2009).
29. J. Bühl, H. Babovsky, A. Kiessling, and R. Kowarschik, "Digital synthesis of multiple off-axis holograms with overlapping Fourier spectra," *Opt. Commun.* **283**, 3631–3638 (2010).
30. V. Mico and Z. Zalevsky, "Superresolved digital in-line holographic microscopy for high resolution lensless biological imaging," *J. Biomed. Opt.* **15**, 046027 (2010).
31. L. Granero, V. Micó, Z. Zalevsky, and J. García, "Synthetic aperture superresolved microscopy in digital lensless Fourier holography by time and angular multiplexing of the object information," *Appl. Opt.* **49**, 845–857 (2010).
32. C. Yuan, G. Situ, G. Pedrini, J. Ma, and W. Osten, "Resolution improvement in digital holography by angular and polarization multiplexing," *Appl. Opt.* **50**, B6–B11 (2011).
33. M. Kim, Y. Choi, C. Fang-Yen, Y. Sung, R. R. Dasari, M. S. Feld, and W. Choi, "High-speed synthetic aperture microscopy for live cell imaging," *Opt. Lett.* **36**, 148–150 (2011).
34. A. Calabuig, V. Mico, J. Garcia, Z. Zalevsky, and C. Ferreira, "Single-exposure super-resolved interferometric microscopy by RGB-multiplexing," *Opt. Lett.* **36**, 885–887 (2011).
35. H. Li, L. Zhong, Z. Ma, and X. Lu, "Joint approach of the sub-holograms in on-axis lensless Fourier phase-shifting synthetic aperture digital holography," *Opt. Commun.* **284**, 2268–2272 (2011).